Quadrupole-Enhanced Overset Noise Predictions for Counter-Rotating Open Rotors

Enrico Fabiano[1], Andrew C. Kirby[1,2], Zhi Yang[1], and Dimitri J. Mavriplis*[1,2]

[1] *Scientific Simulations LLC, Laramie, WY, USA*
[2] *University of Wyoming, Laramie, WY, USA*

This paper presents the development of a quadrupole-enhanced acoustic-analogy approach for the prediction of the noise levels generated by counter-rotating open rotors. In the proposed approach, an overset-based Discontinous Galerkin flow solver is used to resolve the aerodynamic near field. The CFD solution is then used as input to a source-time-dominant, integral solution of the Ffowcs Williams - Hawkings equation for far-field noise propagation. This noise propagation strategy is based on the evaluation of surface and volume integrals, demonstrating the feasibility of the direct integration of the quadrupole term in the Ffowcs Williams - Hawkings equation. The proposed acoustic-analogy approach is used to compute the aerodynamic near-field and the far-field noise signatures of the F31/A31 counter-rotating open rotor configuration. The aerodynamic and acoustic predictions are validated by comparison with available experimental data.

I. Introduction

Compliance with community-noise regulations is one of the primary challenges to the development of a successful contra-rotating open-rotor (CROR) engine concept. The design of these propulsion systems has traditionally focused on optimizing the aerodynamic performance of the rotors, while assessing the far-field noise levels later in the design process, typically via expensive fly-over model testing. Turbulence scale-resolving noise simulations can provide cost-effective alternatives to model testing earlier in the design phase, particularly when leveraging the most recent high-performance computing architectures. In eddy-resolving simulations, the complex unsteady flowfield around a CROR geometry is used as input to a Ffowcs Williams - Hawkings (FW-H) acoustic integration procedure to determine the noise signature of the rotors at the certifications points. In this work we present the application of our unstructured overset CFD solver and of our quadrupole-enhanced FW-H acoustic analogy to the prediction of the noise generated by installed CROR geometries at far-field acoustic observers. In our overset approach,[1] the unstructured NSU3D flow solver[2] is used to model the flow field in the vicinity of the counter-rotating rotor, while the wake regions are resolved using the CartDG high-order, adaptive, Cartesian, DG flow solver.[3] Unstructured near-body grids greatly simplify the meshing process, particularly for the modeling of complex configurations, and allow for the use of highly anisotropic grid elements to resolve the blade boundary layers. On the other hand, the Cartesian discretization inherently ensures the grid isotropy necessary to prevent generation of grid-induced spurious noise typical of anisotropic structured and unstructured meshes.[4] For far-field acoustic predictions, the near-field flow solution is then used as input to our time-domain implementation of the FW-H integration[5] to determine the acoustic signatures at far-field observers. The source-time-dominant implementation[6,7] of the FW-H integration follows Farassat's formulation 1A[8] and employs the modifications of di Francescantonio[9] to allow for the evaluation of the acoustic integrals on a permeable integration surface. In the proposed FW-H integration, the acoustic integrals are evaluated in parallel by leveraging the domain-decomposition and parallel-execution strategy of the underlying CFD solver. At regular intervals during the CFD time-integration process, the total noise levels are computed by summing the acoustic-pressure contributions from each compute core of the CFD solver using the Message-Passing Interface (MPI) protocol. Furthermore, by computing the acoustic integrals as part of the CFD time-marching procedure, our approach

*Professor, Department of Mechanical Engineering. Fellow AIAA. mavripl@uwyo.edu

avoids the need to write the flow-solution history to disk, and enables the direct evaluation of the volume integral of the FW-H equation.

The paper is structured as follows: Section II describes the CFD solver and the proposed acoustic-integration approach. After validation of the quadrupole-enhanced FW-H integration, Section III presents the application of the proposed acoustic-analogy approach to the prediction of the far-field noise signatures of the F31/A31 Historical Blade Set[10] at low-speed conditions.[10–12] Finally, Section IV draws conclusions and highlights future work.

II. Solver Description

In this section we introduce the component of our acoustic-analogy approach. An overset, compressible discontinuous Galerkin flow solver is used to compute the flow-solution history in the aerodynamic near field. The CFD solution is then propagated to far-field observers using a quadrupole-enhanced, time-domain formulation of the integral FW-H equation.

II.A. High-Order Overset CFD Solver

The CFD solution in the aerodynamic near field is computed using a dual-mesh, dual-solver paradigm[1] where an unstructured near-body solver is coupled to a Cartesian, adaptive discontinuous Galerkin off-body solver using an overset domain connectivity algorithm. In the near-body, the second-order accurate, finite-volume NSU3D flow solver[2] enables the modeling of complicated geometries through the use of highly-stretched unstructured grids. The solver employs a BDF2 implicit time-integration approach to alleviate the numerical difficulties associated with the small mesh spacings in boundary layer regions. In the off-body region, the Cartesian DG solver[3] guarantees mesh isotropy in the near-field that, together with the employed non-linearly stable, low-dissipation, total-kinetic-energy-preserving DG discretization,[13] is essential for the accurate resolution of the acoustic waves. Additionally, resolution of the near-field can be further enhanced using a local Adaptive Mesh Refinement (AMR) approach capable of increasing the mesh resolution, the order of accuracy of the DG discretization, or a combination of both approaches. Designed for computational efficiency, the off-body DG scheme relies on an explicit 4th order accurate Runge-Kutta time-stepping scheme that enables the efficient resolution of the sound waves in the acoustic near-field. Communication of the near-body and off-body flow solvers is accomplished through the TIOGA overset domain connectivity algorithm.[14] The near-body and off-body solvers iterate in time in an uncoupled manner, and a global time orchestrates when data is exchanged between the two solvers. For aeroacoustic simulations, the global time is chosen to ensure the desired frequency resolution of the noise spectra.

Simulation of high-Reynolds-number turbulent flows is accomplished using a hybrid Reynolds-averaged Navier-Stokes/Large-Eddy Simulation (RANS/LES) strategy: a Delayed-Detached-Eddy Simulation (DDES) approach based on the Spalart-Allmaras turbulence model[15] is used in the near-wall region resolved by the unstructured mesh. In the off-body region, the noise-generating turbulent structures are resolved by a dynamic Smagorinsky sub-grid scale LES approach implemented in the off-body Cartesian DG solver.

This high-order, overset CFD flow solver, named `dg4est`, has been validated on canonical problems such as the Taylor-Green vortex problem[16] and extensively applied to the simulation of wake-dominated turbulent flows such as fixed-wing,[17] rotorcraft,[18] propeller[19] and wind energy applications.[20]

II.B. FW-H acoustic analogy

Despite the continuous increase in computational resources, numerical simulations that resolve wave propagation from the near field to far-field observers are still impractical. Hence, a viable approach to predicting far-field noise levels is the use of hybrid methods that have been developed over the years[6] and are now fairly well established. In hybrid methods, the finely resolved near-field flow time history is leveraged by an acoustic formulation that predicts the noise radiated to a given observer. The acoustic analogy implemented in this work is based on the integral solution to the FW-H equation. In this approach, the `dg4est` off-body CFD solver provides the near-field flow time-history to the FW-H acoustic integration module that propagates the acoustic pressure to the far-field observers.

Originally developed for rotorcraft applications,[5] the integral solution to the FW-H equation follows formulation 1-A[8] of Farassat, and determines the total acoustic pressure at the observers as the sum of two

surface integrals (monopole and dipole terms) and one volume integral (quadrupole term):

$$p'(\mathbf{y},t) = p'_{\mathrm{T}}(\mathbf{y},t) + p'_{\mathrm{L}}(\mathbf{y},t) + p'_{\mathrm{Q}}(\mathbf{y},t) \tag{1}$$

In this work, the FW-H acoustic integration has been implemented in the Cartesian off-body solver, and the

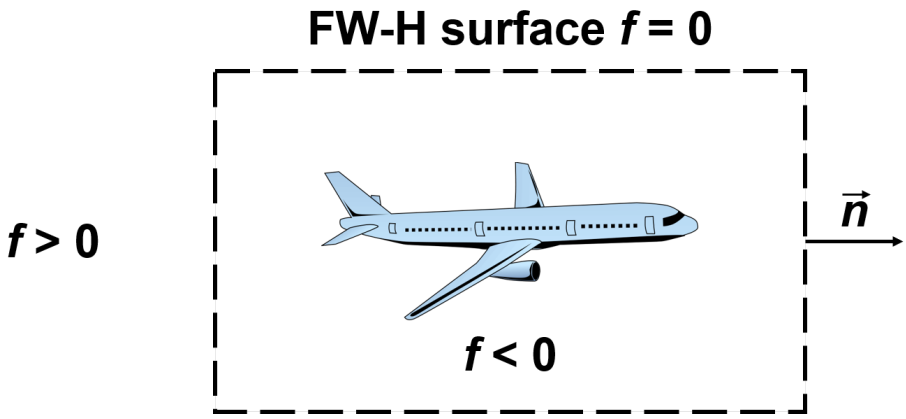

Figure 1. Schematics of the permeable-surface integration approach.

formulation for the surface integrals follows the approach proposed by di Francescantonio.[9] In this approach, shown schematically in Fig. 1, the surface integrals are evaluated on a permeable integration surface and they are given by

$$\begin{aligned}
4\pi p'_T(\mathbf{y},t) &= \int_{f=0} \left[\frac{\rho_o \left(\dot{U}_n + U_{\dot{n}} \right)}{r(1-M_r)^2} \right]_{\text{Ret.}} dS \\
&+ \int_{f=0} \left[\frac{\rho_o U_n K}{r^2(1-M_r)^3} \right]_{\text{Ret.}} dS \\
4\pi p'_L &= \frac{1}{c_o} \int_{f=0} \left[\frac{\dot{L}_r}{r(1-M_r)^2} \right]_{\text{Ret.}} dS \\
&+ \int_{f=0} \left[\frac{L_r - L_M}{r^2(1-M_r)^2} \right]_{\text{Ret.}} dS \\
&+ \frac{1}{c_o} \int_{f=0} \left[\frac{L_r K}{r^2(1-M_r)^3} \right]_{\text{Ret.}} dS
\end{aligned} \tag{2}$$

where the monopole and dipole terms take the form

$$\begin{aligned}
U_i &= \left(1 - \frac{\rho}{\rho_o} \right) v_i + \frac{\rho u_i}{\rho_o} \\
L_i &= p' n_i + \rho u_i \left(u_n - v_n \right)
\end{aligned} \tag{3}$$

and the quantities in the acoustic integrals' kernels are defined as

$$\begin{aligned}
U_{\mathrm{n}} &= U_i n_i \\
M_{\mathrm{r}} &= M_i r_i \\
L_{\mathrm{r}} &= L_i r_i \\
L_{\mathrm{M}} &= L_i M_i \\
K &= r\dot{M}_r + c_o(M_r - M^2)
\end{aligned} \tag{4}$$

In eq. (2-4), $f = 0$ is the permeable integration surface, n_i is the outward surface normal vector, v_i is the local velocity of the surface and $M_i = v_i/c_o$ is the surface Mach number vector. Furthermore, the distance

between the far-field observer $\mathbf{y}$ and an acoustic source $\mathbf{x}$ on the integration surface is $r_i = y_i - x_i$, ρ_o and c_o are the freestream density and speed of sound, ρ is the local fluid density and u_i is the local fluid velocity relative to the surface. Finally, $p' = p - p_o$ is the local fluid pressure relative to the freestream pressure, and $\dot{(\ )}$ represents time differentiation with respect to the source time.

The quadrupole term consists of a volume integration in the region $f > 0$ outside of the permeable integration surface

$$4\pi p'_Q(\mathbf{y},t) \quad = \quad \int_{f>0} \left[\frac{K_1}{c_o^2 r} + \frac{K_2}{c_o r^2} + \frac{K_3}{r^3} \right]_{\text{Ret.}} dV \tag{5}$$

where the terms K_1, K_2 and K_3 are

$$\begin{aligned}
K_1 &= \frac{\ddot{T}_{\text{rr}}}{(1-M_{\text{r}})^3} + \frac{\ddot{M}_{\text{r}} T_{\text{rr}} + 3\dot{M}_{\text{r}}\dot{T}_{\text{rr}}}{(1-M_{\text{r}})^4} + \frac{3\dot{M}_r^2 T_{\text{rr}}}{(1-M_{\text{r}})^5} \\
K_2 &= \frac{-\dot{T}_{ii}}{(1-M_{\text{r}})^2} - \frac{4\dot{T}_{\text{Mr}} + 2T_{\dot{\text{M}}\text{r}} + \dot{M}_{\text{r}} T_{ii}}{(1-M_{\text{r}})^3} \\
&\quad + \frac{3\left(1-M^2\right)\dot{T}_{\text{rr}} - 6\dot{M}_{\text{r}} T_{\text{Mr}} - 3M_i\dot{M}_i T_{\text{rr}}}{(1-M_{\text{r}})^4} + \frac{6\dot{M}_{\text{r}}\left(1-M^2\right)T_{\text{rr}}}{(1-M_{\text{r}})^5} \\
K_3 &= \frac{2T_{\text{MM}} - \left(1-M^2\right)T_{ii}}{(1-M_{\text{r}})^3} - \frac{6\left(1-M^2\right)T_{\text{Mr}}}{(1-M_{\text{r}})^4} + \frac{3\left(1-M^2\right)^2 T_{\text{rr}}}{(1-M_{\text{r}})^5}
\end{aligned} \tag{6}$$

In eq. (6) M_i is the Mach number vector of a volume source, and the term T_{ij} is the Lighthill's stress tensor

$$T_{ij} \quad = \quad \rho u_i u_j + \left(p' - c_o^2 \rho'\right)\delta_{ij} - \tau_{ij} \tag{7}$$

where $\rho' = \rho - \rho_o$, δ_{ij} is the Kronecker delta, and τ_{ij} is the local shear stress tensor. Furthermore, $T_{\text{rr}} = T_{ij} r_i r_j$ is the double contraction of Lighthill's tensor and the remaining terms are defined as

$$\begin{aligned}
T_{\text{MM}} &= T_{ij} M_i M_j & T_{\text{Mr}} &= T_{ij} M_i r_j & T_{\dot{\text{M}}\text{r}} &= T_{ij}\dot{M}_i r_j \\
\dot{T}_{\text{Mr}} &= \dot{T}_{ij} M_i r_j & \dot{T}_{\text{rr}} &= \dot{T}_{ij} r_i r_j & \ddot{T}_{\text{rr}} &= \ddot{T}_{ij} r_i r_j
\end{aligned}$$

To allow for a seamless coupling of the acoustic module with the CFD time integration process, the integrals in eqs. (2) and (5) are evaluated using a source-time-dominant algorithm[6,7] described by eq. (8)

$$t = \tau + r(\mathbf{x}(\tau), \mathbf{y}(t))/c_0 \tag{8}$$

For every source time τ, the acoustic waves will reach the observer at reception time t after traveling the distance $r(\mathbf{x}(\tau), \mathbf{y}(t))$ between the source $\mathbf{x}$ at the emission time τ and the observer $\mathbf{y}$ at reception time t, and eq. (8) is solved using Garrick's triangle.[21] The source time in eq. (8) is the CFD time and the integrals in eqs. (2) and (5) are evaluated at every time step or at regular intervals during the CFD time-integration process.

The acoustic integration surface is a user-specified closed surface located in the off-body solver at an approximate fixed distance from the body. For the integration of the quadrupole term, the integration volume corresponds to the entire computational domain outside of the permeable integration surface. Every degree of freedom of the underlying CFD discretization on the integration surface or in the exterior volume corresponds to an acoustic source. At regular time intervals in the CFD time integration process, the kernels in equations (2) and (5) are assembled from the kinematics of the acoustic source and the computed CFD solution is passed to the acoustic module via shared memory pointers. In both the near-body and the off-body solvers, the first time derivative for the flow variables used in the acoustic integrals is computed using the spatial residual of the CFD discretization

$$\frac{dQ}{dt} = -R(Q(t)) \tag{9}$$

where $Q(t)$ is the discrete solution vector and $R(Q(t))$ is the residual vector. Furthermore, the second time derivative of the flow quantities are computed using an Euler-explicit finite-difference scheme

$$\frac{d^2Q}{dt^2} = \frac{R^{n+1} - R^n}{\Delta t} \tag{10}$$

Finally, the total acoustic pressure at the far-field observers is reconstructed using a linear interpolation strategy. This strategy requires storing only the acoustic pressure at the observers and is performed every time the acoustic integrals are evaluated.

II.B.1. Validation of the Acoustic Analogy

The flow over a sphere is used to validate the proposed acoustic-analogy approach. The sphere has unit radius, the uniform, freestream Mach number is M=0.3, and the Reynolds number based on the radius of the sphere is Re=10,000. The overset grid system consists of a trimmed, near-body mesh and a statically-refined off-body grid. The near-body unstructured mesh contains 100,000 nodes and has an outer radius of $2R$, where R is the radius of the sphere. The Cartesian off-body grid extends $[-512, 512]R$ in the three coordinate directions with a resolution of 0.125, and contains 1,231,707 elements. The order of accuracy of the DG discretization varies from 3^{rd}-order in the mesh overlap region to 4^{th}-order in the wake of the sphere. The noise prediction is based on the integration of surface and volume terms of the FW-H equation. The surface integrals are evaluated on a permeable surface in the off-body grid that extends four sphere radii in the upwstream, downstream and lateral directions, as shown in Fig. 2(a). The volume integrals are evaluated in the computational domain that surrounds the integration surface. Validation of the acoustic integration is performed by comparing the propagated noise levels to the sound pressure computed by the `dg4est` flow solver for an observer at $(5.12, -4.75, -4.75)R$. The choice of a near-field observer is dictated by the need to minimize the numerical dissipation of the acoustic waves in the CFD solution. Figure 2(b)

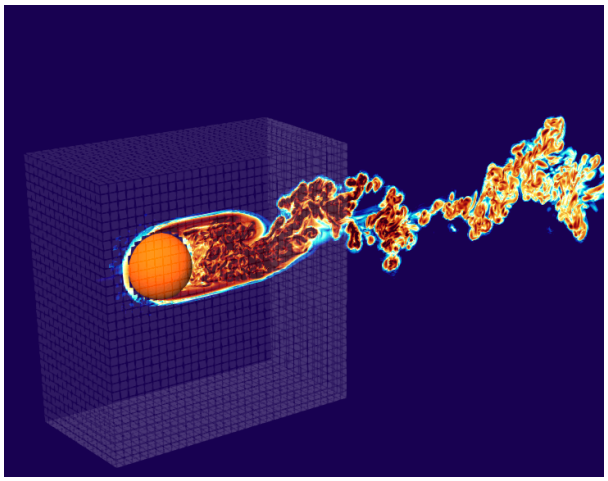

(a) Validation of the quadrupole-enhanced acoustic analogy approach for the flow over a sphere.

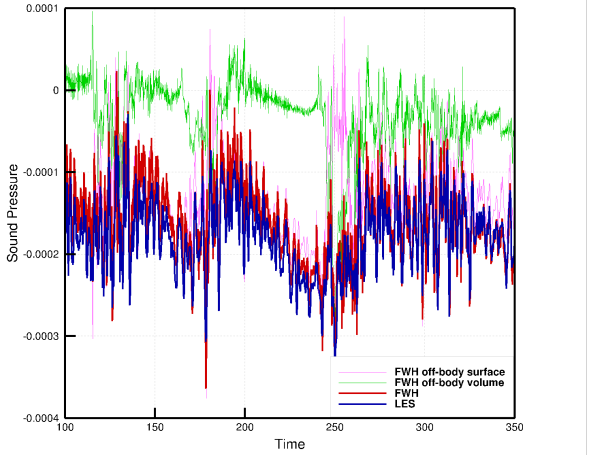

(b) Surface, volume and total acoustic pressures at the observer and comparison with direct noise computation for the flow over a sphere.

Figure 2. Unsteady flow over a unit sphere used for the validation of the acoustic integration in NSU3D.

shows the comparison of computed and propagated sound pressures at the observer. The acoustic pressure propagated by the surface integrals greatly overpredicts the direct noise computation, particularly when turbulent structures cross the permeable integration surface, resulting in spurious noise. However, the combination of surface and volume integrals in the FW-H propagation accurately reconstructs the noise signature computed by the CFD solver, validating the implementation of our acoustic analogy approach.

III. Results

After successful validation, the proposed acoustic-analogy approach has been used to compute the low-speed noise signatures of the the F31/A31 Historical Blade Set.[10] This CROR configuration consists of 12 blades in the forward rotor and 10 blades in the aft rotor, as shown in Fig. 3(a). Each rotor blade is discretized by an unstructured mesh that is replicated, translated, and rotated to the initial azimuthal angle within each rotor configuration. Additionally, the hub geometry is fitted with an independent unstructured

near-body grid. The mixed-elements near-body grids consists of a total of 58 million nodes and the wall spacing has been chosen to achieve a y^+ value close to 1 at the operating Reynolds number. The off-body grid system overlaps the unstructured grids in the vicinity of the rotor, as shown in Fig. 3(b). The Cartesian off-body grid is composed of 13 levels of refinement spanning a computational domain of $[-3072, 3072]^3$ [in], consisting of 4.9 million elements overall. The coarsest level is composed of an $8 \times 8 \times 8$ mesh of resolution 768.0 [in], and the finest level has a resolution of 0.1875 [in]. The static mesh is refined *a priori* to resolve the flow features in the vicinity of the rotor and in the wake region, as shown in Fig. 4. Furthermore, two different *p-refinement* strategies are employed in the off-body grid system. The first strategy uses a uniform 2^{nd}-order spatial accuracy with $p = 1$ elements, totaling 39 million degrees of freedom. The second *p-refinement* strategy uses a mixed p-degree approach: on the finest mesh level, $p = 1$ elements are used to match the solution accuracy and mesh resolution in the outer near-body grid. As the mesh levels are coarsened moving away from the overlap region, the solution accuracy is increased up to $p = 3$, totaling 185 million degrees of freedom (DOF). The total number of degrees of freedom for the two overset grid systems is summarized in Table 1

	p-refinement 1	*p-refinement* 2
Near-body dof.	58	58
Off-body dof.	39	185
Total dof.	97	243

Table 1. Near-body, off-body and total number of degrees of freedom (dof), in millions, for the two *p-refinement* strategies used in this work.

To enable the comparison of our simulations to experimental data, the flow conditions considered in this work correspond to the conditions of the low-speed experimental campaign performed in the 9-*ft.* $\times$ 15-*ft.* NASA Low-Speed Wind Tunnel.[10–12] In these experiments the free-stream Mach Number is $M = 0.2$ with an angle of attack of zero degrees. The Reynolds number based on standard density and pressure at 15°C, inflow velocity and average rotor diameter of 25.225 inches is $Re = 2.95$ million. Three rotor speeds, shown in Table 2, are considered in this work ranging from the approach RPM to the nominal takeoff RPM. For all simulations, the temporal resolution corresponds to an azimuthal angle of 0.25° rotation of the

Case	Mach	RPMC
1	0.20	4620
2	0.20	5551
3	0.20	6436

Table 2. RPM corrected for sea-level conditions for the F31/A31 CROR geometry considered in this work.

rotor. The CFD time-integration process is initiated with freestream flow conditions. In all the simulations, the aerodynamic quantities are evaluated during the first 4 rotor revolutions. The acoustic pressure is accumulated over 20 rotor revolutions starting from the 15th revolution to wash out initial transient effects.

III.A. Aerodynamic Results

The two *p-refinement* strategies result in nearly identical aerodynamic quantities of interest, so that only one set of results is presented in this section. Figure 5 compares the aerodynamic predictions from our high-order overset solver with the data from the NASA 9×15 low-speed wind tunnel experimental campaign,[10] as well as the results from the NASA OVERFLOW and FUN3D solvers.[11] Overall, our aerodynamic results have similar characteristics to the OVERFLOW and FUN3D results, particularly at 6436 RPM. The thrust force results compare favorably with the experimental data and with the other simulations at all RPM speeds. Similar to the other simulations, the torque ratio comparison with experimental data is less favorable, as the ratio diverges from wind- tunnel data as the rotor speed decreases to 4620 RPM. This behavior is somewhat expected as the blade pitch angle settings deviate from design point as the rotation rate is reduced, potentially leading to increased flow separation. Additionally, flow separation may be more sensitive to grid resolution effects at these conditions,[11] and a grid-refinement study for the near-body blade grids will be performed in future work. Finally, Fig. 6 shows the force-convergence histories for the 5551 RPM case, illustrating the

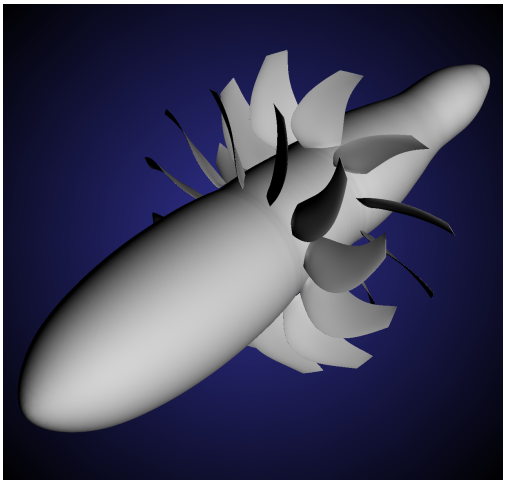

(a) F31/A31 counter-rotating open rotor geometry

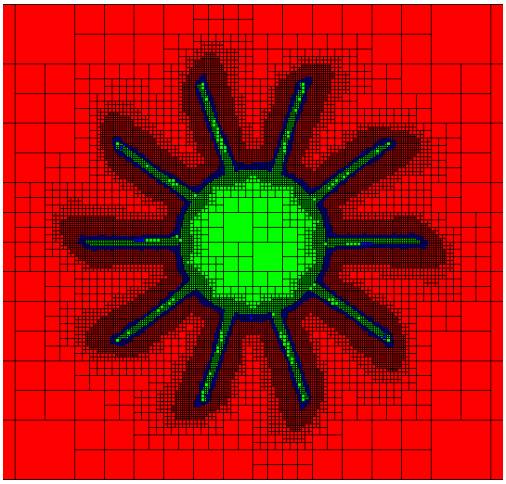

(b) Aft rotor overset connectivity pattern

Figure 3. CROR Configuration.

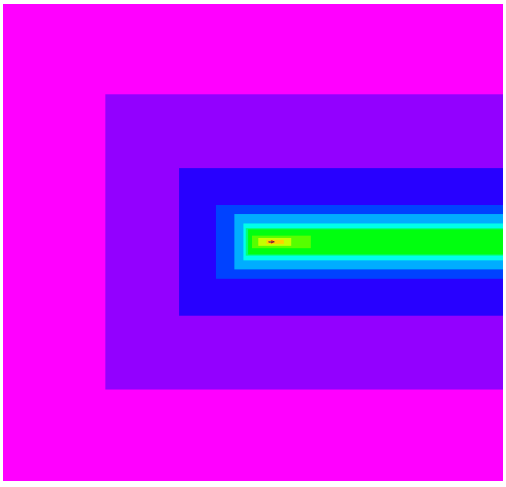

(a) Off-Body Mesh Domain

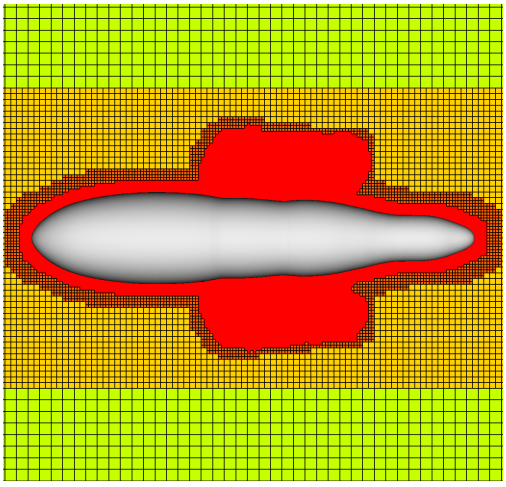

(b) Off-Body Adaptive Mesh

Figure 4. Statically-refined off-body grid system: magenta (coarsest mesh level) to red (finest mesh level). In the overset region, the resolution of the off-body grid is adaptively refined to match the resolution of the near-body unstructured grid.

fast convergence to force equilibrium after a few rotor revolutions. The convergence history for the other RPM cases listed in Table 2 is similar to the convergence for the 5551 RPM case.

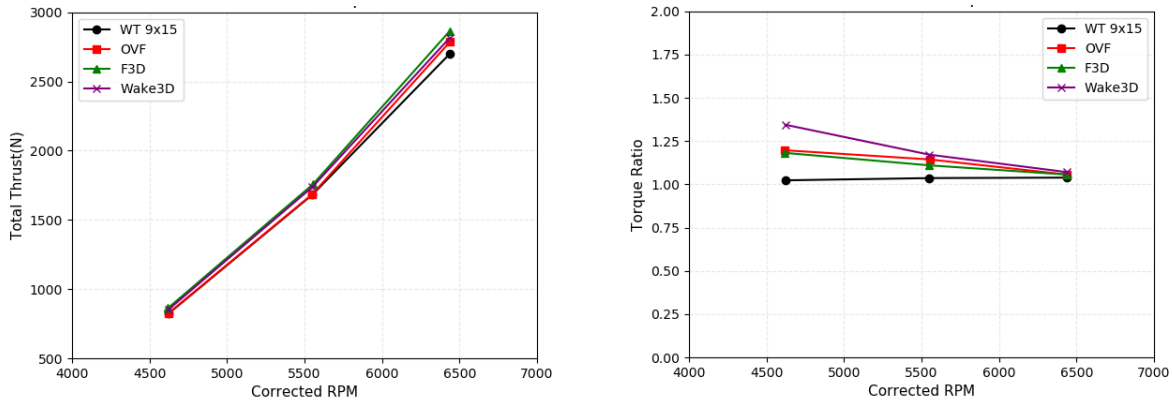

(a) Thrust force.

(b) Torque force ratio (fwd/aft).

Figure 5. CROR force comparisons with experimental data and simulation results. [WT 9x15 – Experiment, OVF – OVERFLOW, F3D – FUN3D, Wake3D – this work]

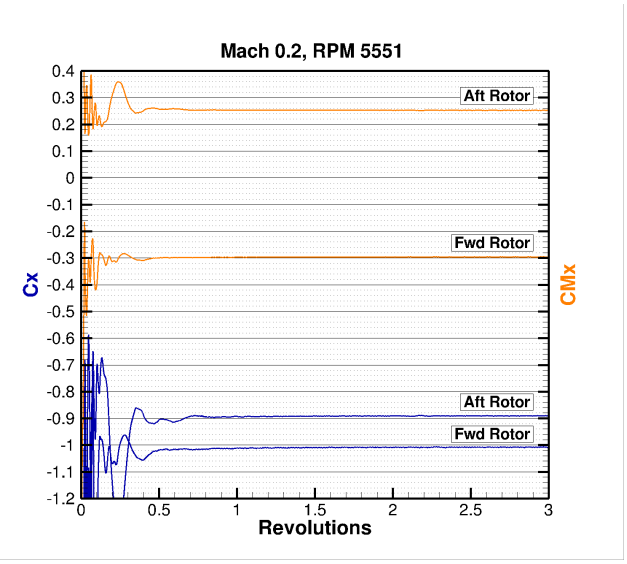

Figure 6. Convergence history of forces and moments on the F31/A31 CROR configuration at 5551 RPM for the first *p-refinement* strategy.

III.B. Acoustic Results

In this section we present the far-field propagation of the near-field solutions around the F31/A31 for the $RPM = 6436$ case. The noise spectra at the far-field observers are compared to the experimental data from the NASA 9x15 Low Speed Wind Tunnel test,[10,12] and Fig. 7 shows the location of the observers with respect to the counter-rotating open rotor.[10,12]

We perform two noise propagations using the two different *p-refinement* strategies in the off-body Cartesian grid. For both noise predictions, the surface acoustic integrals are evaluated on a permeable surface in the off-body grid surrounding the rotor geometry, shown in Fig. 8, and the volume integrals are performed in the entire computational domain outside of the acoustic integration surface. In order to compute the acoustic time histories at the far-field observers, we performed the acoustic integration for 20 rotor revolutions. Welch's method[22] is then used to compute the Sound Pressure Level (SPL) spectra after dividing the pressure time histories into 8 overlapping segments with 50% overlap, and the tones are identified following a strategy similar to the peak-finding algorithm in reference.[11]

III.B.1. Propagation 1

The first noise propagation has been performed using the CFD solution computed using the first *p-refinement* strategy described above. In this strategy, the off-body mesh is discretized using $p = 1$ elements, resulting in second-order accuracy for the off-body solver. In order to asses the contribution of the quadrupole term to the far-field acoustic spectra, Fig. 9 compares the SPL values at the acoustic observers for the shaft orders SO-10 and S0-12, and demonstrates the importance of the volume contributions to the noise spectra, particularly for observers at shallow angles from the rotor axis. Fig. 10 depicts the OASPL computed using the combined surface and volume integration terms at the different observer locations, compared with experimental values and results obtained by the OVERFLOW and FUN3D flow solvers.[11] Since at second-order accuracy the off-body mesh contains considerably less resolution than the OVERFLOW and FUN3D grids,[11] the OASPL levels are somewhat underpredicted compared to the levels from the NASA solvers.

The SPL at the acoustic observers for different shaft orders is shown in Fig. 11 and Fig. 12, together with a comparison with available experimental[10,12] and computational[11] data. There is good agreement between propagated and experimental noise values for our first acoustic propagation. The noise levels for shaft orders 10 and 12 are well predicted, and the over prediction for the 30-degree observer is associated with the quadrupole term and requires further investigation. The trend in noise levels for the higher shaft orders are well predicted, but the absolute noise levels are under predicted as a consequence of the 2nd-order accuracy of the overset grid system used in this noise propagation.

III.B.2. Propagation 2

The second noise propagation uses the second *p-refinement* strategy described above, and employes a high-order discretization (up to p=3 or fourth order accurate) of the off-body Cartesian grid. All the noise spectra presented in this section consist of the combination of surface and volume integrals.

Figure 13 shows the directivity plot for the second acoustic prediction, and demonstrates good agreement with available experimental[10,12] and computational[11] data, indicating higher overall sound pressure levels using the more accurate discretization. In particular, the SPL at the acoustic observers for the higher shaft orders is shown in Fig. 14. At the higher shaft orders, the noise propagation is in significantly better agreement with experimental data as a consequence of the fourth-order accurate discretization in the off-body grid of the overset grid system.

Finally, Fig. 15 shows SPL as a function of frequency for different sideline angles for both runs, confirming that the high-order discretization of the off-body grid enables the accurate prediction of the sound pressure levels at higher shaft orders.

III.B.3. Computational Cost

In this section we present the computational cost of one time step of our simulation. A total of 24 meshes are used in our simulations, including 23 unstructured near-body meshes with a total of 58 million nodes and one adapted Cartesian mesh with 39 million degrees of freedom for the first *p-refinement* strategy, and 185 million degrees of freedom for the second *p-refinement* strategy. Each near-body rotor blade mesh is partitioned across 72 CPU cores, and the near-body CROR body mesh is partitioned across 108 CPU cores, totaling 1,692 cores. The off-body adaptive Cartesian mesh is distributed to 216 CPU cores and 864 CPU cores for the first and second *p-refinement* strategy, for a total of 1,908 CPU and 2,556 CPU cores

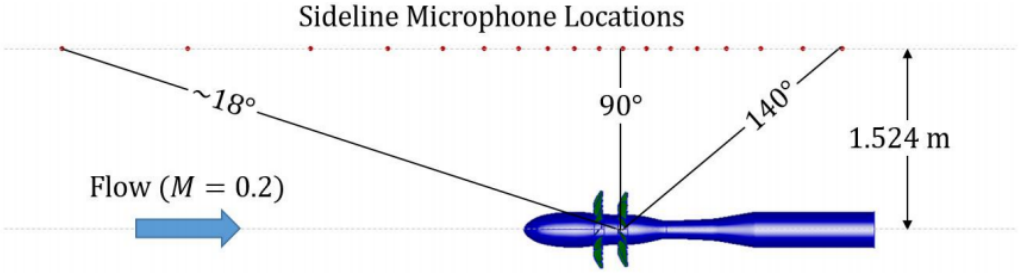

Figure 7. Schematic of observer locations in the NASA 9x15-ft. Low Speed Wind Tunnel.[11]

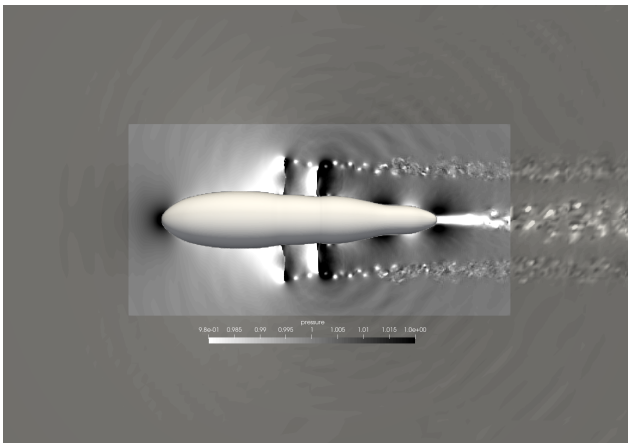

Figure 8. Schematic of a permeable acoustic integration surface superimposed on the instantaneous hybrid RANS/LES solution around the CROR configuration.

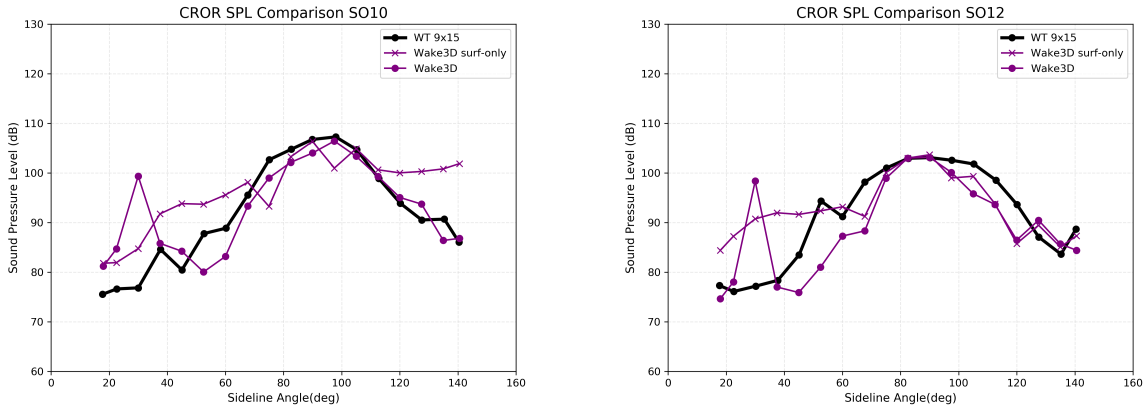

Figure 9. Surface and combined (surface and volume) SPL for shaft orders 10 and 12 at the acoustic observers.

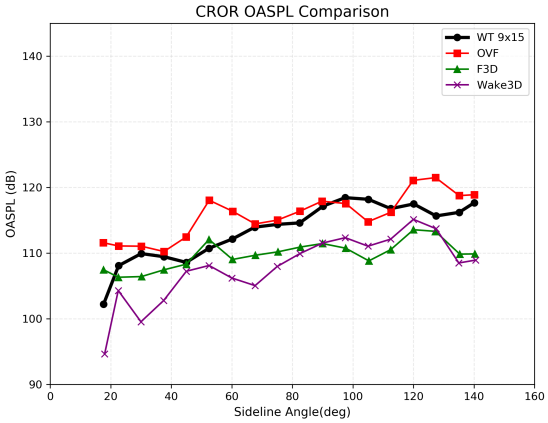

Figure 10. Overall sound pressure level (OASPL) for the first acoustic propagation.

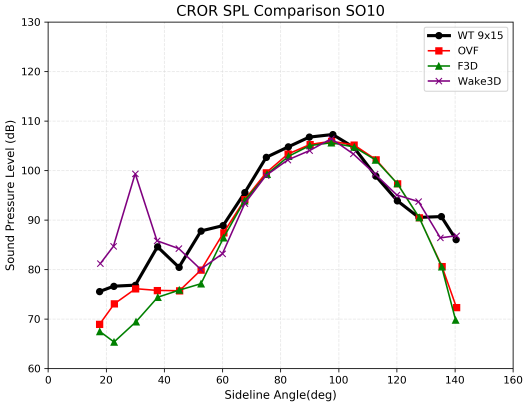

(a) Shaft order 10.

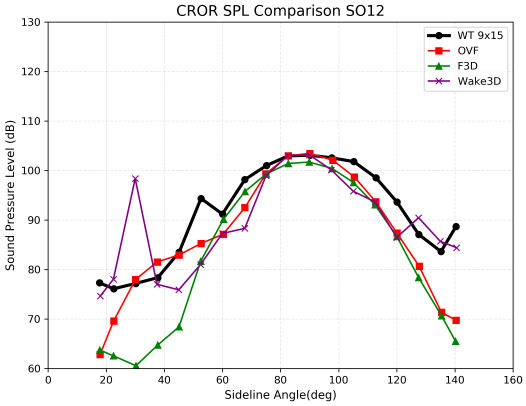

(b) Shaft order 12.

Figure 11. SPL for shaft order 10 and 12 for the first acoustic propagation, and comparison to experimental[10,12] and computational[11] data.

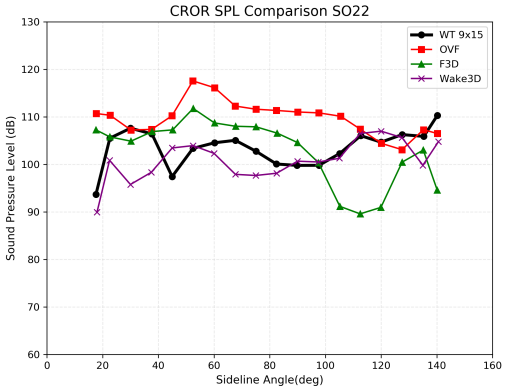

(a) Shaft order 22.

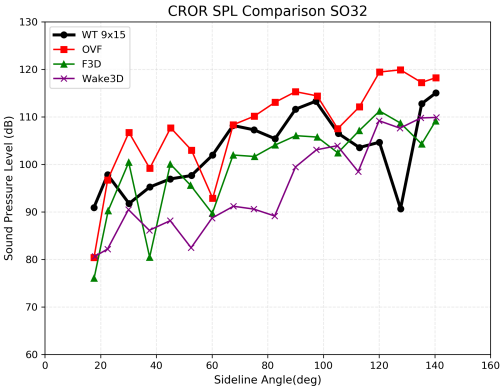

(b) Shaft order 32.

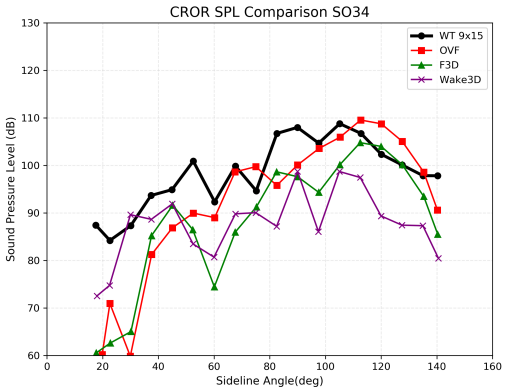

(c) Shaft order 34.

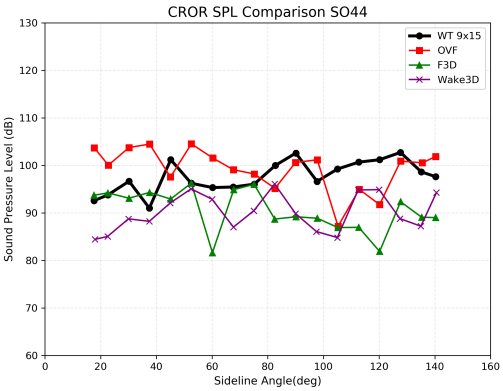

(d) Shaft order 44.

Figure 12. SPL for higher shaft orders for the first acoustic propagation and comparison to experimental[10,12] and computational[11] data.

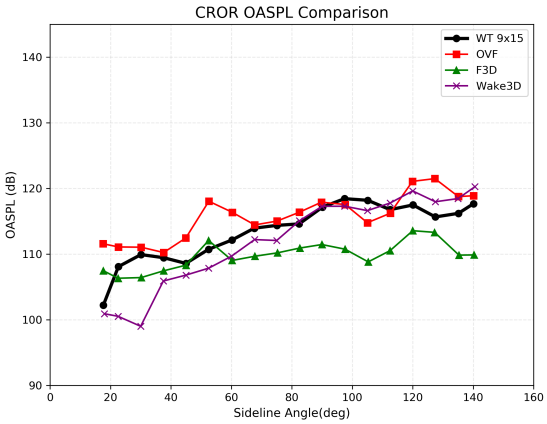

Figure 13. Overall sound pressure level (OASPL) for the second acoustic propagation.

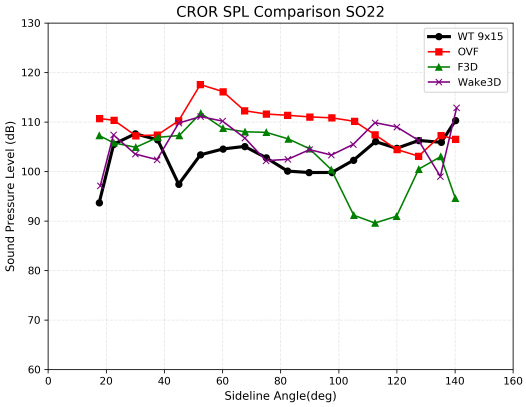

(a) Shaft order 22.

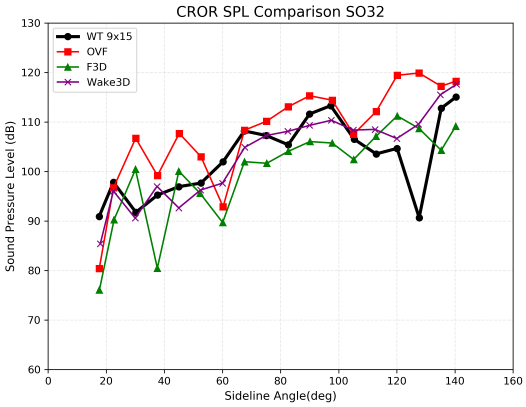

(b) Shaft order 32.

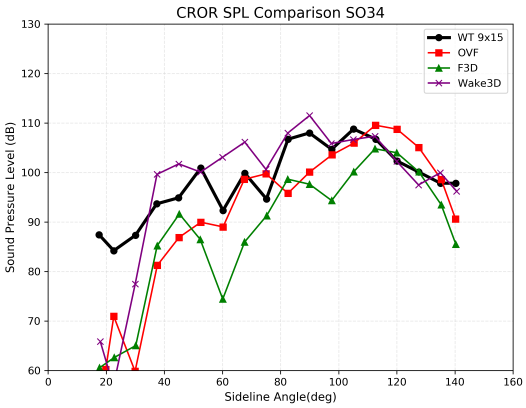

(c) Shaft order 34.

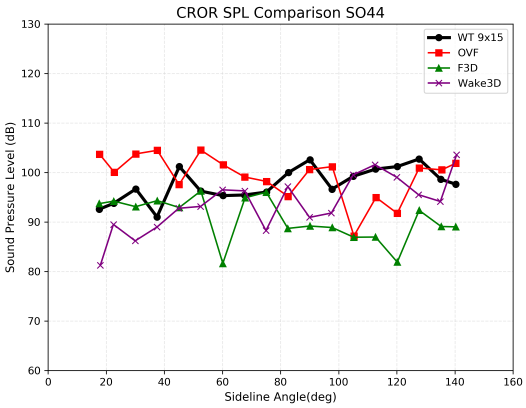

(d) Shaft order 44.

Figure 14. SPL for higher shaft orders for the second acoustic propagation and comparison to experimental[10,12] and computational[11] data.

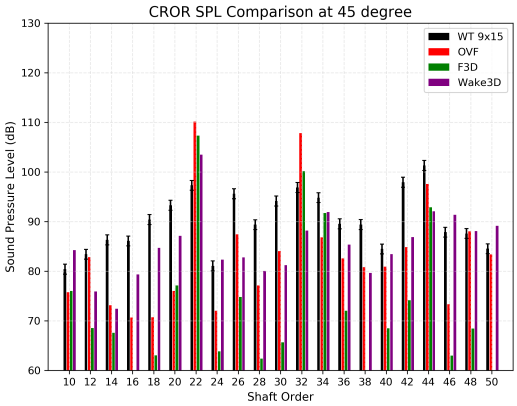

(a) 45° SPL: First acoustic propagation.

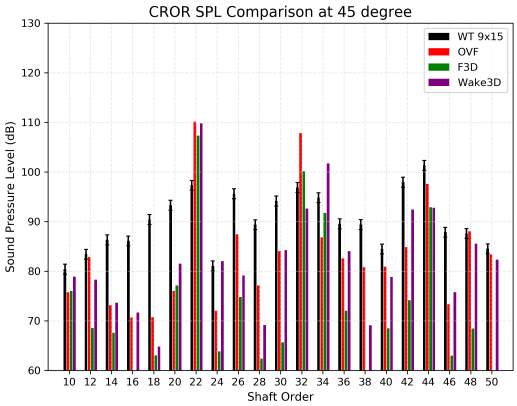

(b) 45° SPL: Second acoustic propagation.

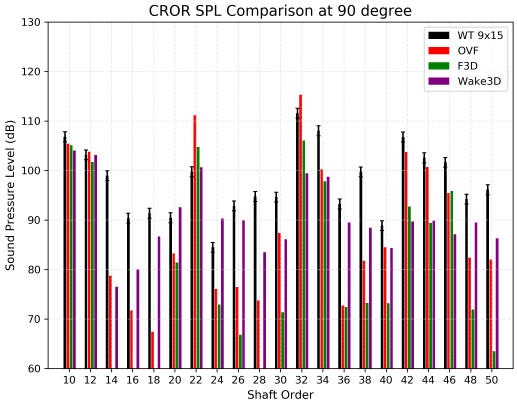

(c) 90° SPL: First acoustic propagation.

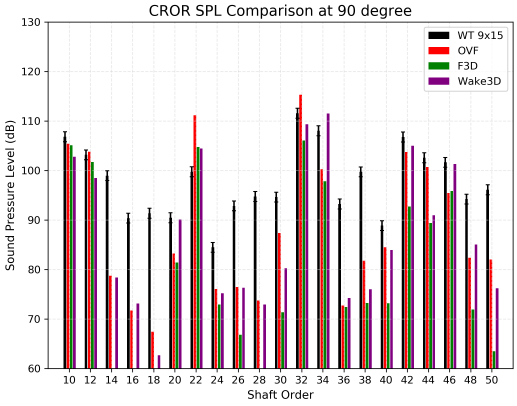

(d) 90° SPL: Second acoustic propagation.

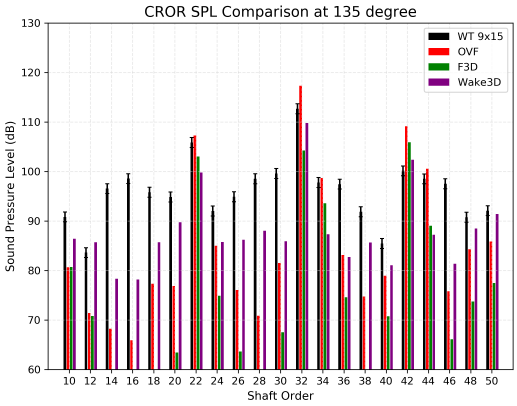

(e) 135° SPL: First acoustic propagation.

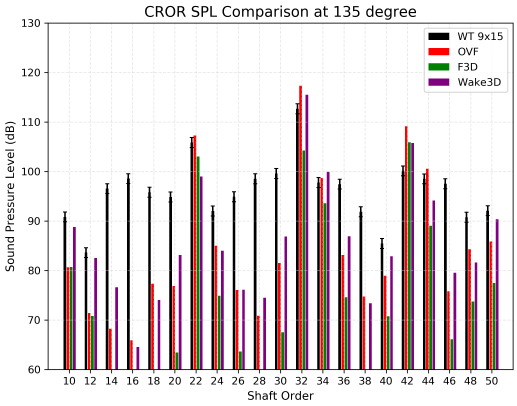

(f) 135° SPL: Second acoustic propagation.

Figure 15. Sound pressure levels (SPL) for first *p-refinement* (2^{nd}-order accuracy) and second *p-refinement* strategy (4^{th}-order accuracy), and comparison to experimental[10,12] and computational[11] data.

respectively. One time step of our simulation consists of the computation of the overset connectivity, the computation of one time step in our high-order CFD solver, and of the evaluation of the surface and volume integrals of the FW-H equation. Table 3 provides the breakdown of the wall-clock time of a 0.25° time step for each run. Overall, a total simulation time of four hours is required to perform one rotor revolution using our framework, and the wall clock time for the two runs is similar. However, the second *p-refinement* strategy uses more CPU cores due to the higher number of degrees of freedom in the off-body mesh. The overset connectivity for our simulations takes nearly 50% of the wall-clock time of one time step.

Test Case	Overset sec/Δt	CFD sec/Δt	FW-H sec/Δt	Time Per Rev
CROR - strategy 1	4.98	5.07	0.45	4.2 (hrs)
CROR - strategy 2	4.93	5.02	0.47	4.2 (hrs)

Table 3. Computational cost of the overset connectivity, high-order overset flow solver, and quadrupole-enhanced acoustic propagation for 18 observers for the two *p-refinement* strategies.

The FW-H integration predicts noise levels at 18 far-field observers and takes approximately 4.5% of the total cost at each CFD time step. Additionally, Fig. 16 shows an investigation of the computational cost of our acoustic propagation model with respect to the number of acoustic observers for the second *p-refinement* strategy. The FW-H implementation shows very good scalability, particularly up to 100 observers, where the FW-H integration requires approximately 20% of the CFD wall-clock time, or 10% of the total simulation time if the overset mesh assembly time is included. These results demonstrate the feasibility of performing the volume integration of the quadrupole term of the FW-H equation.

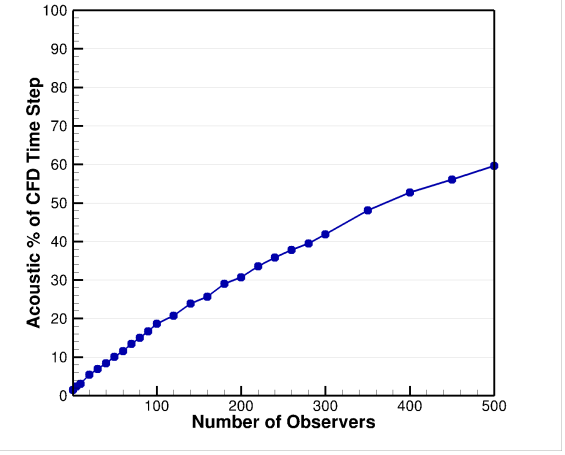

Figure 16. Computational cost of the acoustic propagation relative to one time step versus total simulation time as a function of number of observers.

IV. Conclusion and Future Work

A quadrupole-enhanced, overset-based acoustic-analogy approach has been developed and validated in this work. The acoustic analogy is based on a high-order overset CFD solver, and a quadrupole-enhanced, source-time-dominant integral formulation of the FW-H equation. The flow over a unit sphere has been used to validate the proposed acoustic analogy. The acoustic signature propagated by the FW-H to an observer in the near-field has been compared to a direct noise computation performed with the high-order CFD solver, and excellent agreement has been found between the propagated noise signature and the direct noise computation. Upon validation, the quadrupole-enhanced acoustic-analogy approach has been used to predict the noise signature of the F31/A31 CROR configuration at far-field observers with good success, demonstrating the feasibility of performing the direct integration of the quadrupole term of the FW-H equation. Future work will focus on reducing the computational cost of our acoustic-analogy approach. The cost of computing the overset mesh connectivity can be reduced by using an Exact Inverse Map approach in the donor-search algorithm.[23] Furthermore, the overset connectivity could be precomputed at the beginning

of the simulation at every CFD time step, following an approach developed in similar work.[11] Similarly, to further reduce the computational cost of the quadrupole integration, the source-observer distance can be pre-computed at the beginning of the simulation and retrieved from memory each time the acoustic integrals are evaluated. Finally, the performance of the quadrupole integration can also be improved by refactoring the code and improving its vectorization.

V. Acknowledgements

The authors would like to acknowledge support of NASA through NASA SBIR 2022 Phase-I funding, Contract: 80NSSC22PB178, Proposal: 22-1- A1.02-5606.

References

[1]Brazell, M. J., Kirby, A. C., and Mavriplis, D. J., "A high-order discontinuous-Galerkin octree-based AMR solver for overset simulations," *23rd AIAA Computational Fluid Dynamics Conference*, Jun 05–09 2017, AIAA Paper 2017–3944.

[2]Mavriplis, D. J. and Mani, K., "Unstructured Mesh Solution Techniques using the NSU3D Solver," AIAA Paper 2014-081, 52nd Aerospace Sciences Meeting, National Harbor, MD.

[3]Kirby, A. C., Mavriplis, D. J., and Wissink, A., "An Adaptive Explicit 3D Discontinuous Galerkin Solver for Unsteady Problems," *22nd AIAA Computational Fluid Dynamics Conference*, Jun 22–26 2015, AIAA Paper 2015–3046.

[4]Tam, C. K. W., *Computational Aeroacoustics: a Wave Number Approach*, Cambridge University Press, 2012.

[5]Fabiano, E., Mishra, A., Mavriplis, D. J., and Mani, K., "Time-dependent aero-acoustic adjoint-based shape optimization of helicopter rotors in forward flight," *57th AIAA/ASCE/AHS/ASC Structures, Structural Dynamics, and Materials Conference*, January 4–8 2016, AIAA Paper 2016–1910.

[6]Brentner, K. S. and Farassat, F., "Modeling Aerodynamically Generated Sound of Helicopter Rotors," *Progress in Aerospace Sciences*, Vol. 39, 2003, pp. 83–120.

[7]Casalino, D., "An Advanced Time Approach for Acoustic Analogy Predictions," *Journal of Sound and Vibration*, Vol. 261, No. 4, 2003, pp. 583–774.

[8]Farassat, F. and Succi, G. P., "The prediction of helicopter discrete frequency noise," *Vertica*, Vol. 7-4, 1983, pp. 309–320.

[9]di Francescantonio, P., "A New Boundary Integral Formulation for the Prediction of Sound Radiation," *Vertica*, Vol. 7-4, 1983, pp. 309–320.

[10]Stephens, D. B., "Data Summary Report for the Open Rotor Propulsion Rig Equipped With F31/A31 Rotor Blades," Tech. rep., 2014, NASA/TM—2014-216676.

[11]Nark, D. M., Jones, W., Boyd, D., and Zawodny, N., "Isolated open rotor noise prediction assessment using the F31A31 historical blade set," *54th AIAA Aerospace Sciences Meeting*, January 2016, AIAA Paper 2016-1271.

[12]Sree, D., "Far-Field Acoustic Power Level and Performance Analyses of F31/A31 Open Rotor Model at Simulated Scaled Takeoff, Nominal Takeoff, and Approach Conditions: Technical Report I," Tech. rep., 2015, NASA/CR—2015-218716.

[13]Gassner, G. J., Winters, A. R., and Kopriva, D. A., "Split form nodal Discontinuous Galerkin Schemes with Summation-By-Parts Property For The Compressible Euler Equations," *Journal of Computational Physics*, Vol. 327, 2016, pp. 39–66.

[14]Roget, B. and Sitaraman, J., "Robust and Efficient Overset Grid Assembly for Partitioned Unstructured Meshes," *Journal of Computational Physics*, Vol. 260, 2014, pp. 1–24.

[15]Spalart, P. R. and Allmaras, S. R., "A One-equation Turbulence Model for Aerodynamic Flows," *La Recherche Aérospatiale*, Vol. 1, 1994, pp. 5–21.

[16]Stoellinger, M. K., Edmonds, A. P., Kirby, A. C., Mavriplis, D. J., and Heinz, S., "Dynamic SGS modeling in LES using DG with kinetic energy preserving flux schemes," *57th AIAA Aerospace Sciences Meeting*, January 07–11 2019, AIAA Paper 2019–1648.

[17]Mavriplis, D. J., Bogstad, M., and Kirby, A., "RANS and Hybrid RANS-LES Results for the Fourth High-Lift Prediction Workshop using the NSU3D Solver," AIAA Paper 2022-3810, AIAA SCITECH 2022 Forum, San Diego, CA., January 2022.

[18]Kara, K., Kirby, A. K., and Mavriplis, D. J., "Hover Predictions Using a High-Order Discontinuous Galerkin Off-Body Discretization," *AIAA Scitech 2020 Forum*, January 6–10 2020, AIAA Paper 2020–0771.

[19]Yang, Z., Kirby, A., and Mavriplis, D., "Comparison of Propeller-Wing Interaction Simulation using Different Levels of Fidelity," *AIAA Scitech Meeting*, January 2022, AIAA Paper 2022–1678.

[20]Kirby, A. C., Brazell, M. J., Yang, Z., Roy, R., Ahrabi, B. R., Stoellinger, M. K., Sitaraman, J., and Mavriplis, D. J., "Wind farm simulations using an overset hp-adaptive approach with blade-resolved turbine models," *The International Journal of High Performance Computing Applications*, Vol. 33, No. 5, 2019, pp. 897–923.

[21]Garrick, I. E. and Watkins, C. E., "A theoretical study of the effect of forward speed on the free-space sound-pressure field around propellers," Tech. Rep. TR 1198, NACA, 1954.

[22]Welch, P., "The use of fast Fourier transform for the estimation of power spectra: A method based on time averaging over short, modified periodograms," *IEEE transactions on audio and electroacoustics*, Vol. 15, No. 2, 1967, pp. 70–73.

[23]Roget, B. and Sitaraman, J., "Robust and scalable overset grid assembly for partitioned unstructured meshes," *51st AIAA Aerospace Sciences Meeting*, January 2013, AIAA Paper 2013-797.